Self-calibration for Mueller polarimeters based on DoFP polarization imagers

Xiaobo Li, François Goudail, Shih-Chi Chen

Self-calibration for Muller polarimeters based on DoFP polarization imagers

XIAOBO LI[1,3], FRANÇOIS GOUDAIL[2,4], AND SHIH-CHI CHEN[1,3,5]

[1] Department of Mechanical and Automation Engineering, The Chinese University of Hong Kong, Shatin, N.T., Hong Kong SAR , China
[2] Université Paris-Saclay, Institut d'Optique Graduate School, CNRS, Laboratoire Charles Fabry, 91120, Palaiseau, France
[3] Centre for Perceptual and Interactive Intelligence, Shatin, N.T., Hong Kong SAR, China
[4] francois.goudail@institutoptique.fr
[5] scchen@mae.cuhk.edu.hk

Compiled January 10, 2022

Mueller polarimeters (MPs) based on division of focal plane (DoFP) polarization imagers can achieve fast measurements and significantly improve the effectiveness of Mueller polarimetry. In this Letter, we demonstrate a unique property of the DoFP sensor-based MPs: They can be calibrated without any extra polarizing reference element. We describe a self-calibration method that only requires six image acquisitions; based on our analysis, the calibration accuracy is only limited by the noise. ©

http://dx.doi.org/10.1364/ao.XX.XXXXXX

Mueller matrix (MM) provides important information about the interaction of materials with polarized light and physical properties, including smoothness, microstructure, texture, etc. [1–3]. The measurement and analysis of MM have a wide variety of applications, ranging from morphology detection to clinicopathologic analysis [4–6]. A typical Mueller polarimeter (MP) configuration, as shown in Fig. 1(a), is based on a CCD or CMOS camera and dual-rotating retarders [7, 8]. A new type of MP has been proposed by replacing the standard camera with a division of focal plane (DoFP) polarization image sensor, whose configuration is shown in Fig. 1 (b). This design can achieve fast imaging/measurement and significantly improve the effectiveness of MM measurements [9, 10]. Recently, Huang et al. reported a complete MM microscope based on dual DoFP imagers, which has the capability of imaging the MM of samples in real-time [9]. In this Letter, we aim to demonstrate another unique function of DoFP-based MPs: They can be self-calibrated without any extra polarizing reference element.

The fundamental model of MPs is:

$$\mathbb{I} = \mathbb{A}\left(\alpha_2, \delta_2, \theta_2\right) \cdot \mathbb{M} \cdot \mathbb{G}\left(\alpha_1, \delta_1, \theta_1\right), \tag{1}$$

where $\mathbb{I}$ denotes the matrix of the captured intensity measurements; $\mathbb{M}$ is the MM to be measured; and $\mathbb{G}$ and $\mathbb{A}$ are the measurement matrices of the polarization state generator (PSG) and the polarization state analyzer (PSA), respectively, which are functions of angles of the polarizers (α_1, α_2), angles of the retarders (θ_1, θ_2), and their retardances (δ_1, δ_2). The accuracy of MM measurement requires exact values of these parameters.

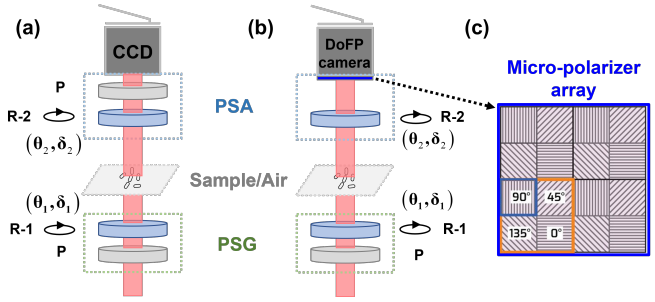

Fig. 1. MP configurations based on (a) a traditional CCD; and (b) a commercial DoFP polarization camera. P: polarizer, R: retarder. (c) Enlarged view of the micro-polarizer array.

In general, the polarizer angles are stable, but the parameters related to retarders may vary due to environmental disturbances, e.g., temperature fluctuations. Accordingly, in DoFP-based MPs, (θ_1, θ_2) and (δ_1, δ_2) often treated as unknowns, which require experimental calibration. All existing methods to calibrate MPs require an extra calibration step with standard reference components or samples, e.g., calibrated polarizers or retarders [11–14]. An effective self-calibration method without additional polarizing elements is highly desirable. Recently, we have developed a few methods for self-calibrating the retardance or axis orientation of the retarder in Stokes polarimeters [15, 16]. Although these methods can handle a single parameter, MPs depend on more than four parameters that need to be calibrated simultaneously. Besides, the Stokes vector has only four elements whereas the MM has 16, which makes the calibration process complex and challenging. In this Letter, we present a new self-calibration method for DoFP-based MPs, which can estimate all unknown parameters of the retarders without introducing any additional polarizing elements.

In our method, the first step is to calibrate the PSA parameters $(\delta_2,\ \theta_2)$ using the redundancy of intensity measurements in a DoFP camera [17]. As such, we set the direction of the PSG retarder (R-1) to $\vartheta = \theta_1 + \gamma_0$, where θ_1 refers to the true retarder direction with a nominal value of 0° (Note that the value of θ_1 is unknown here.), and γ_0 is the known angular increment of R-1.

The generated Stokes vector can be expressed in Eq. (2).

$$\mathbf{S}_{in} = \frac{qI_0}{2}\begin{bmatrix} 1 \\ \cos^2 2\vartheta + \cos\delta_1 \sin^2 2\vartheta \\ (1-\cos\delta_1)\sin 2\vartheta \cos 2\vartheta \\ \sin\delta_1 \sin 2\vartheta \end{bmatrix} \quad (2)$$

where q denotes the quantum efficiency of the camera, which is typically set to one for simplicity, and I_0 is the intensity level of the light source. In the absence of samples, the PSA directly observes $\mathbf{S}_{in}$. To measure $\mathbf{S}_{in}$, the direction θ_2 of the PSA retarder (R-2) needs to changeN_2 times, where $N_2 \geq 2$. Since the DoFP imager has four different polarizer orientations, the measured intensity vector $\mathbf{I}$ in Eq. (3) has $4N_2 \times 1$ elements.

$$\mathbf{I} = \mathbb{A}\left(\delta_2, \theta_2\right)\mathbf{S}_{in} + \mathbf{n}, \quad (3)$$

where $\mathbf{n}$ denotes the additive white Gaussian noise with a variance of σ^2. In order to simultaneously estimate $\mathbf{S}_{in}$ and $\boldsymbol{\eta} = (\delta_2, \theta_2)$ without any additional polarizing elements, we first express the log-likelihood function of this problem as:

$$\ell(\mathbf{S}_{in}, \boldsymbol{\eta}) = -\frac{1}{2\sigma^2}\|\mathbf{I} - \mathbb{A}(\boldsymbol{\eta})\mathbf{S}_{in}\|^2. \quad (4)$$

Next, we denote the parameters to be estimated as a vector $\mathbf{p} = (\mathbf{S}_{in}, \boldsymbol{\eta})$. We first investigate the feasibility of estimating $\mathbf{p}$ by analyzing the Fisher information matrix, whose elements have the following expression:

$$\mathbb{F}_{ij} = -\left\langle \frac{\partial^2 \ell}{\partial p_i \partial p_j} \right\rangle = \frac{1}{\sigma^2}\left(\mathbf{S}_{in}^T \frac{\partial \mathbb{A}^T}{\partial p_i}\frac{\partial \mathbb{A}}{\partial p_j}\mathbf{S}_{in}\right), \quad (5)$$

where $\langle\cdot\rangle$ denotes ensemble averaging over the noise realizations. The Cramer-Rao lower bound (CRLB) for estimation of p_i, $i \in \{1, 6\}$ is the diagonal elements $\left[\mathbb{F}^{-1}\right]_{ii}$, which represents the lower bound of the estimation variance of p_i with an unbiased estimator [15]. Similar to the derivation steps in Ref. [18], the inverse of the Fisher matrix can be derived as $\mathbb{F}^{-1} = \begin{bmatrix}\mathbb{B} & \mathbb{C}; & \mathbb{C}^T & \mathbb{D}\end{bmatrix}$, where $\mathbb{D}$ is the covariance matrix of the estimation of $\mathbf{S}_{in}$; $\mathbb{C}$ is the cross-covariance matrix of $\mathbf{S}_{in}$ and $\boldsymbol{\eta}$; and $\mathbb{B}$ is presented in Eq. (6), where the CRLB of η_i is the i^{th} diagonal element of $\mathbb{B}$. To realize self-calibration, i.e., estimation of $\boldsymbol{\eta}$, $\mathbb{B}$ has to be invertible.

$$\mathbb{B}_{ij} = \left[\left(\mathbb{P}_A^{\perp}\frac{\partial \mathbb{A}}{\partial \eta_i}\mathbf{S}_{in}\right)^T\left(\mathbb{P}_A^{\perp}\frac{\partial \mathbb{A}}{\partial \eta_j}\mathbf{S}_{in}\right)\right]^{-1}\sigma^2, \quad (6)$$

In Eq. (6), $\mathbb{P}_A^{\perp} = \mathbb{E} - \mathbb{A}\left(\mathbb{A}^T\mathbb{A}\right)^{-1}\mathbb{A}^T$ ($\mathbb{E}$ is the identity matrix) is the projection matrix orthogonal to the space spanned by the columns of $\mathbb{A}$.

To assess the validity of the self-calibration property for a given experimental configuration, we define the "condition matrices" as $\mathbb{Q}_i = \mathbb{P}_A^{\perp}\frac{\partial \mathbb{A}}{\partial \eta_i}$. It has been shown in Ref. [18] that to enable self-calibration, the input polarization states should depend on the rank of $\mathbb{Q}_i$. Moreover, after derivation, we find that $\text{rank}\left(\mathbb{Q}_{\theta_2}\right) = 3$ and $\text{rank}\left(\mathbb{Q}_{\delta_2}\right) = 2$ when the number of different PSA states satisfies $N_2 \geq 3$. This means that the null space for $\mathbb{Q}_{\theta_2}$ is empty and that the null space of $\mathbb{Q}_{\delta_2}$ is one dimensional. It can be shown that the null space of $\mathbb{Q}_{\delta_2}$ is spanned by the Stokes vectors with degree of linear polarization (DoLP) = 0, i.e., $S_1 = S_2 = 0$. In other words, the self-calibration of retarder orientation is always feasible, but the self-calibration of retardance cannot be achieved if $\mathbf{S}_{in}$ is purely circularly polarized. Hence, to accurately estimate the θ_2, the value of γ_0 should be chosen to such that the generated $\mathbf{S}_{in}$ is not circularly polarized.

Interestingly, this self-calibration method does not work for the MP based on traditional cameras as shown in Fig. 1 (a). This is because in this case, $\text{rank}\left(\mathbb{Q}_{\delta_2}\right) = 0$ and $\text{rank}\left(\mathbb{Q}_{\theta_2}\right) = 1$, which means that self-calibration of δ_2 is impossible for any input Stokes vector [18]. Besides, since only the fourth column of the condition matrix $\mathbb{Q}_{\delta_2}$ is nonzero, self-calibration of θ_2 is impossible for any purely linear input Stokes vector [16].

Next, we investigate the precision of $\boldsymbol{\eta}$ and $\mathbf{S}_{in}$ when self-calibration is feasible. We assume that the acquisition of N_2 is performed by setting the directions of R-2 to $\theta_2 + (i-1)\cdot\pi/N_2$ ($i \in [1, N_2]$), where the true value of R-2's initial direction θ_2 is unknown. This is the optimal combination for estimating $\mathbf{S}_{in}$ because it can minimize the equally weighted variance (EWV) metric, which is defined as the trace of matrix $\mathbb{V} = (\mathbb{A}^T\mathbb{A})^{-1}$ [3]. Based on this setting, the closed-form CRLB expressions of δ_2 and θ_2 can be obtained as:

$$\begin{aligned} \text{CRLB}[\delta_2] &= \frac{4(1+c)}{\mathcal{N}(1-c)\mathcal{L}^2}, \\ \text{CRLB}[\theta_2] &= \frac{1+c}{\mathcal{N}\left[(1-c)^2\mathcal{L}^2 + 2(1-c^2)\mathcal{C}^2\right]} \end{aligned} \quad (7)$$

where $c = \cos^2\delta_2$; $\mathcal{N} = N_2 \cdot \text{SNR}^2$; $\text{SNR} = I_0/\sigma$; $\mathcal{C} = [S_{in}]_3/[S_{in}]_0$ and $\mathcal{L} = ([S_{in}]_1^2 + [S_{in}]_1^2)^{1/2}/[S_{in}]_0$ respectively denote the degree of circular polarization (DoCP) and DoLP of $\mathbf{S}_{in}$. Under these definitions, $[S]_i$ denotes the $i+1^{th}$ element of $\mathbf{S}$. Notably, Eq. (7) is consistent with our previous analysis, i.e., the calibration of δ_2 does not work when $\mathcal{L} = 0$; and the calibration of θ_2 does not work only when the degree of polarization (DoP) is equal to zero.

With the assumptions of $N_2 = 3$ and $\text{SNR} = 10\sqrt{2}$, Fig. 2 (a) presents the calculated values of $\text{CRLB}^{1/2}[\delta_2]$ and $\text{CRLB}^{1/2}[\theta_2]$ in Eq. (7) as a function of $\mathcal{L}$. It is observed that as $\mathcal{L}$ increases, the estimation precision of δ_2 and θ_2 improves and degrades respectively. This means that it is necessary to optimize the input (by tuning the parameter γ_0) to balance the estimation precisions of δ_2 and θ_2. Figure. 2 (b) presents the estimation performance of both parameters as a function of the true value of δ_2, ranging from 60° to 120°, where one may find that the proposed calibration method has good stability and is robust around $\delta_2 = 90°$. Moreover, when $\delta_2 \in [80°, 100°]$, i.e., a suitable dynamic range of a common quarter-wave plate (QWP), the $\text{CRLB}^{1/2}$ values of θ_2 and δ_2 do not exceed 2.5° and 4.9°, respectively. In particular, for a purely linear $\mathbf{S}_{in}$ with $\mathcal{L} = 1$, one has $\text{CRLB}^{1/2}[\delta_2] = 2\,\text{CRLB}^{1/2}[\theta_2]$, which is also consistent with the analysis in Eq. (7).

Equation (8) presents the CRLB values for each Stokes element, which are obtained from the diagonal elements of $\mathbb{D}$.

$$\text{CRLB}\left[S_{in}\right]_{i-1} = \sigma^2\left\{\mathbb{V}_{ii} + \frac{\left[\sum_n \mathbb{A}^+\frac{\partial \mathbb{A}}{\partial \eta_n}\mathbf{S}_{in}\right]_i^2}{\sum_{m,n}\left(\mathbb{P}_A^{\perp}\frac{\partial \mathbb{A}}{\partial \eta_m}\mathbf{S}_{in}\right)^T\left(\mathbb{P}_A^{\perp}\frac{\partial \mathbb{A}}{\partial \eta_n}\mathbf{S}_{in}\right)}\right\} \quad (8)$$

After simplifying, one obtains:

$$\text{CRLB}\left[S_{in}\right]_{i-1} = \sigma^2\left\{\mathbb{V}_{ii} + \frac{[x_i + y_i]^2}{\text{CRLB}[\delta_2] + \text{CRLB}[\theta_2]}\right\} \quad (9)$$

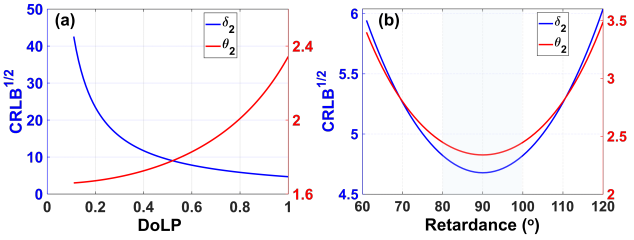

Fig. 2. CRLB$^{1/2}$ as a function of (a) the DoLP when $\delta_2 = 88°$; and (b) the retardance, range from 60° to 120°. Here, $N_2 = 3$; and SNR $= 10\sqrt{2}$.

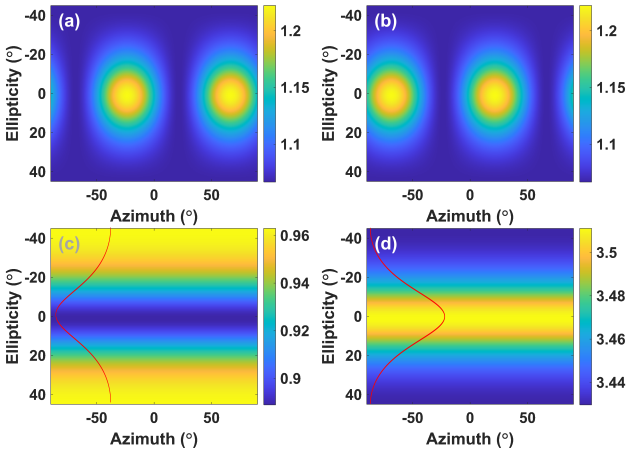

Fig. 3. CRLB value as a function of the azimuth and ellipticity of the input Stokes vector for the estimation of (a) S_1, (b) S_2, (c) S_3, and (d) CRLB$_{\mathcal{S}}$. Here, we set $\delta_2 = 120°$ and $N_2 = 3$ for the ease of comparison.

where

$$x = a\,[0, [S_{in}]_2, -[S_{in}]_1, 0]^T,$$
$$y = [0, -b\,[S_{in}]_1, -b\,[S_{in}]_2, d\,[S_{in}]_3]^T. \quad (10)$$

In Eq. (10), $a = \frac{2(1-\sqrt{c})^2}{1+c}$, $b = \frac{\sqrt{c-c^2}}{1+c}$, and $d = \sqrt{\frac{c}{1-c}}$. The total value is calculated and expressed in Eq. (11).

$$\mathrm{CRLB}_{\mathcal{S}} = \sigma^2 \left\{ \frac{11 - 6c - c^2}{1 - c^2} + \frac{\left(a^2 + b^2\right)\mathcal{L}^2 + d^2\mathcal{C}^2}{\mathrm{CRLB}[\delta_2] + \mathrm{CRLB}\,[\theta_2]} \right\}, \quad (11)$$

To clearly show how the input Stokes vector affects the estimation precision, we calculate the CRLB values for CRLB$[S_{in}]_i (i \in [1,3])$, and the sum CRLB$_{\mathcal{S}}$ in Fig. 3 (a) - 3 (d) respectively, where CRBL is a function of the azimuth and ellipticity of $\mathbf{S}_{in}$. In particular, we see that CRLB$_{\mathcal{S}}$ shown in Fig. 3 (d) only depends on the ellipticity of $\mathbf{S}_{in}$.

As the discussion of CRLBs only represent the lower bounds on the estimation variance, we will next develop a algorithm to estimate $\boldsymbol{\eta} = (\theta_2, \delta_2)$. Based on Ref. [15], it can be shown that the maximum-likelihood estimation of $\boldsymbol{\eta}$ can be achieved by solving Eq. (12):

$$\hat{\boldsymbol{\eta}} = \arg\min_{\boldsymbol{\eta}} \mathcal{F}(\boldsymbol{\eta}), \text{ with } \mathcal{F}(\boldsymbol{\eta}) = \left\| \left(\mathbb{E}_{4N_2} - \mathbb{A}\left(\boldsymbol{\eta}\right)\mathbb{A}^{+}\left(\boldsymbol{\eta}\right)\right)\mathbf{I} \right\|^2. \quad (12)$$

Based on the solution, we can estimate the input Stokes vector by Eq. (13).

$$\hat{\mathbf{S}}_{in} = [\mathbb{A}(\hat{\boldsymbol{\eta}})]^{+}\mathbf{I}, \quad (13)$$

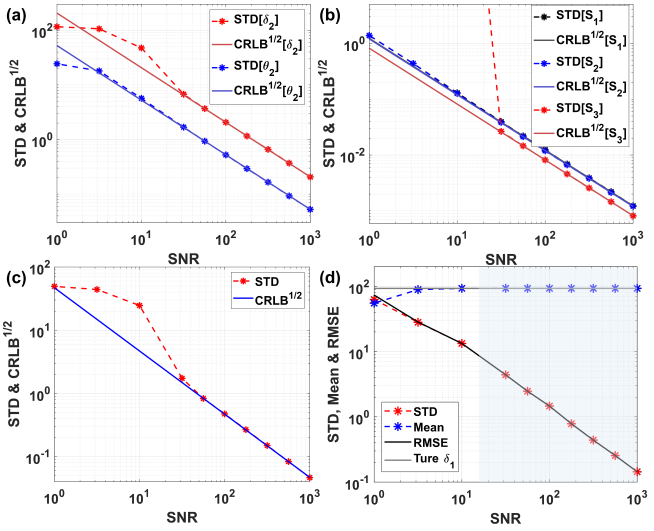

Fig. 4. CRLB$^{1/2}$ and STD as a function of SNR for the estimations of (a) δ_2 and θ_2, (b) S_i, $i \in [1,3]$, and (c) θ_1. (d) STD, mean, and RMSE values as a function of SNR for the estimation of δ_1. Here, $\delta_1 = 93°$, $\delta_2 = 88°$, $s_0 = 1$, $\theta_1 = 2.6°$, $\theta_2 = 2°$, and $\gamma_0 = 22.5°$.

where the superscript $+$ denotes the Moore–Penrose pseudo-inverse matrix [15, 19].

It is important to check whether this algorithm can reach the estimation variance predicted by the CRLB. For this purpose, we compute the estimation standard deviation (STD) of δ_2 and θ_2 via Monte Carlo (MC) simulations on 10^3 noise realizations; the results are plotted with CRLB$^{1/2}$ as a function of SNR in Fig. 4 (a). Here, we set $\gamma_0 = 22.5°$to generate an input Stokes vector with balanced DoLP and DoCP values. From Fig. 4, we find that the estimated STD fits CRLB$^{1/2}$ well in high SNR regions, and the divergence occurs at SNR $\approx$ 30. Besides, we find that the estimation of θ_2 is easier than δ_2 due to its lower STD. This result is consistent with previous studies in Ref. [15, 16]. Figure 4 (b) presents the MC results for the estimation of $\mathbf{S}_{in}$ (with parameters $\delta_1 = 93°$, $\theta_1 = 2.6°$, and $\gamma_0 = 22.5°$), where one may observe that the STD is also equal to CRLB$^{1/2}$ when SNR larger than 30.

In this section, we present how the PSG parameters $(\delta_1,\ \theta_1)$ can be estimated. We first consider the estimation of R-1's orientation θ_1. To achieve this, two different input Stokes vectors ($\mathbf{S}_{in,1}$ and $\mathbf{S}_{in,2}$ as expressed in Eq. (2)) are generated by setting the direction of R-1 to $\vartheta_1 = \theta_1 + \gamma_0$ and $\vartheta_2 = \theta_1 + \gamma_0 + 45°$, where θ_1 is unknown. From Eq. (12) and Eq. (13), we know that when the estimation of PSA parameters is completed, the input Stokes vectors are simultaneously estimated. As such, θ_1 can be calculated by:

$$\hat{\theta}_1 = \frac{1}{2}\tan^{-1}\left(\left[\hat{\mathbf{S}}_{in,1}\right]_3 / \left[\hat{\mathbf{S}}_{in,2}\right]_3\right) - \gamma_0, \quad (14)$$

Since the estimator $\hat{\theta}_1$ in Eq. (14) is a function of two different estimated Stokes parameters, its CRLB has no closed-form expression. Therefore, we approximate the CRLB by the "Delta method" [20], which is expressed in Eq. (15).

$$\mathrm{CRLB}\,[\theta_1] = \sum_{k=1,2}\left\{\left(\frac{\partial\hat{\theta}_1}{\partial\left[\hat{S}_{in,k}\right]_3}\right)^2 \mathrm{CRLB}\,\left[\hat{S}_{in,k}\right]_3\right\}, \quad (15)$$

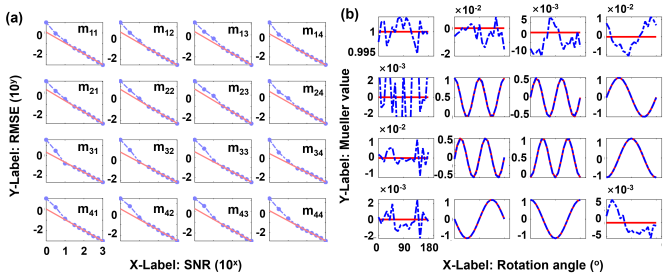

Fig. 5. (a) RMSE values of MM elements as a function of SNR. (b) Estimated values of each MM element as a function of the rotation angle. Dashed line: simulation results; Solid line: theoretical values.

Figure 4 (c) presents the calculated CRLB (from Eq. (15)) and the simulated STD (obtained from MC simulations) as a function of the SNR. It can be seen that the CRLB fits the STD well in high SNR regions, and the divergence occurs at SNR ≈ 30; this is consistent with the results in Fig. 4 (a) and 4 (b).

We next estimate the retardance δ_1 of R-1. From Eq. (13), we have obtained the two input Stokes vectors, which are related to the directions ϑ_k and the retardance δ_1 by Eq. (2). As θ_1 has been estimated by Eq. (14), ϑ_k is known; and we can estimate δ_1 by solving Eq. (16).

$$\mathbf{I}_k = \mathbb{A} \cdot \mathbf{S}_{in,k}\left(\delta_1\right),\ k \in \{1,2\} \tag{16}$$

As it is difficult to obtain a closed-form expression of δ_1 and the related CRLB in Eq. (16), we approach this problem by calculating the STD via MC simulations. The results are presented in Fig. 4 (d) as a function of the SNR. Figure 4 (d) also presents the root-mean-square error (RMSE) to account for the deviation of the estimator's mean value with respect to the true value. From Fig. 4 (d), we observe that the estimation is highly consistent with the true value when the SNR value is higher than 30. Notably, the "divergence point" is the same as other parameters in Fig. 4(a) – 4(c).

In this section, we evaluate the influence of the noise-induced calibration errors on the accuracy of MM measurements. To this aim, we simulate the MM measurement of a QWP oriented at an angle β:

$$\mathbb{M}(\beta) = \frac{1}{2}\begin{bmatrix} 2 & 0 & 0 & 0 \\ 0 & 1+\cos 4\beta & \sin 4\beta & -2\sin 2\beta \\ 0 & \sin 4\beta & 1-\cos 4\beta & 2\cos 2\beta \\ 0 & 2\sin 2\beta & -2\cos 2\beta & 0 \end{bmatrix} \tag{17}$$

Assuming that $\beta = 40°$, we perform MC simulations on 10^3 noise realizations, where at each realization, both the calibration and the MM estimation have been performed. Using the selected parameters in Fig. 4, we plot the estimate RMSE (blue dashed) of each MM element as a function of SNR in Fig. 5 (a). For an ideal MP with perfect calibration, the estimation would be unbiased and the RMSE values of each element M_{ij} would only depend on the noise STD σ and the PSA and PSG matrices $(\mathbb{A}, \mathbb{G})$, as expressed in Eq. (18).

$$\mathrm{R}_{M_{ij}}^{th} = \sigma\left\{\left[\left(\mathbb{A}\otimes\mathbb{G}\right)^T\left(\mathbb{A}\otimes\mathbb{G}\right)\right]^{-1}\right\}_{k,k}. \tag{18}$$

where $\otimes$ is the Kronecker product, and $k = i + 4(j-1)$. For the ease of comparison, we also plot theoretical values (red solid lines) in Fig. 5 (a), where one may observe that the RMSE fits the theoretical value well when the SNR is larger than 30, i.e., when the self-calibration fits its CRLB. Figure 5 (b) presents the estimations of each MM element as a function of the rotation angle β when the SNR is set to 30. From the results, it is observed that the simulations (blue dashed) are in good agreement with the theoretical values (red solid lines) computed from Eq. (18). The results in Fig. 5 suggest that the target MM can be accurately measured via our self-calibration algorithm without any prior knowledge about the retarders in both PSG and PSA.

In conclusion, we have presented a self-calibration method for MPs based on a DoFP camera and two rotating retarders. The method does not require any reference components and is accurate and efficient when the SNR value is above 30. The self-calibration method only requires six acquisitions with different retarder angles; a larger number of acquisitions may be adopted if higher accuracy is needed. The self-calibration method may be applied in MPs with the photon shot noise, which is often the dominant noise source in polarimetry experiments.

Funding. Centre for Perceptual and Interactive Intelligence (CPII) Ltd under the Innovation and Technology Fund (A-CUHK-16-5-14); Innovation Technology Commission (ITC) (ITS/178/20FP).

Disclosures. The authors declare no conflicts of interest.

REFERENCES

1. S. R. Cloude, R. Ossikovski, and E. Garcia-Caurel, IEEE Geosci. Remote. Sens. Lett. **18**, 476 (2020).
2. R. Ossikovski, B. Al Bugami, E. Garcia-Caurel, and S. R. Cloude, Appl. Opt. **59**, 10389 (2020).
3. X. Li, H. Hu, L. Wu, and T. Liu, Opt. Express **25**, 18872 (2017).
4. T. Novikova, A. Pierangelo, S. Manhas, A. Benali, P. Validire, B. Gayet, and A. De Martino, Appl. Phys. Lett. **102**, 241103 (2013).
5. A. Pierangelo, A. Benali, M.-R. Antonelli, T. Novikova, P. Validire, B. Gayet, and A. De Martino, Opt. Express **19**, 1582 (2011).
6. R. Ossikovski and O. Arteaga, JOSA A **36**, 403 (2019).
7. S. Liu, X. Chen, and C. Zhang, Thin Solid Films **584**, 176 (2015).
8. X. Li, F. Goudail, H. Hu, Q. Han, Z. Cheng, and T. Liu, Opt. Express **26**, 34529 (2018).
9. T. Huang, R. Meng, J. Qi, Y. Liu, X. Wang, Y. Chen, R. Liao, and H. Ma, Opt. Lett. **46**, 1676 (2021).
10. J. Qi, C. He, and D. S. Elson, Biomed. Opt. Express **8**, 4933 (2017).
11. E. Compain, S. Poirier, and B. Drevillon, Appl. Opt. **38**, 3490 (1999).
12. S. Bian, C. Cui, and O. Arteaga, Appl. Opt. **60**, 4964 (2021).
13. R. Meng, Z. Chen, X. Wang, Y. Liu, H. He, and H. Ma, Appl. Opt. **60**, 1380 (2021).
14. H. Hu, E. Garcia-Caurel, G. Anna, and F. Goudail, Opt. Lett. **39**, 418 (2014).
15. F. Goudail, X. Li, M. Boffety, S. Roussel, T. Liu, and H. Hu, Opt. Lett. **44**, 5410 (2019).
16. X. Li, F. Goudail, P. Qi, T. Liu, and H. Hu, Opt. Express **29**, 9494 (2021).
17. S. Roussel, M. Boffety, and F. Goudail, Opt. Lett. **44**, 2927 (2019).
18. X. Li, B. Le Teurnier, M. Boffety, T. Liu, H. Hu, and F. Goudail, Opt. Express **28**, 15268 (2020).
19. J. S. Tyo, Appl. Opt. **41**, 619 (2002).
20. J. Benichou and M. H. Gail, The Am. Stat. **43**, 41 (1989).